Volume 13
Number 47
21 December 2025
Pages 23283–23662

Journal of Materials Chemistry C

Materials for optical, magnetic and electronic devices

rsc.li/materials-c

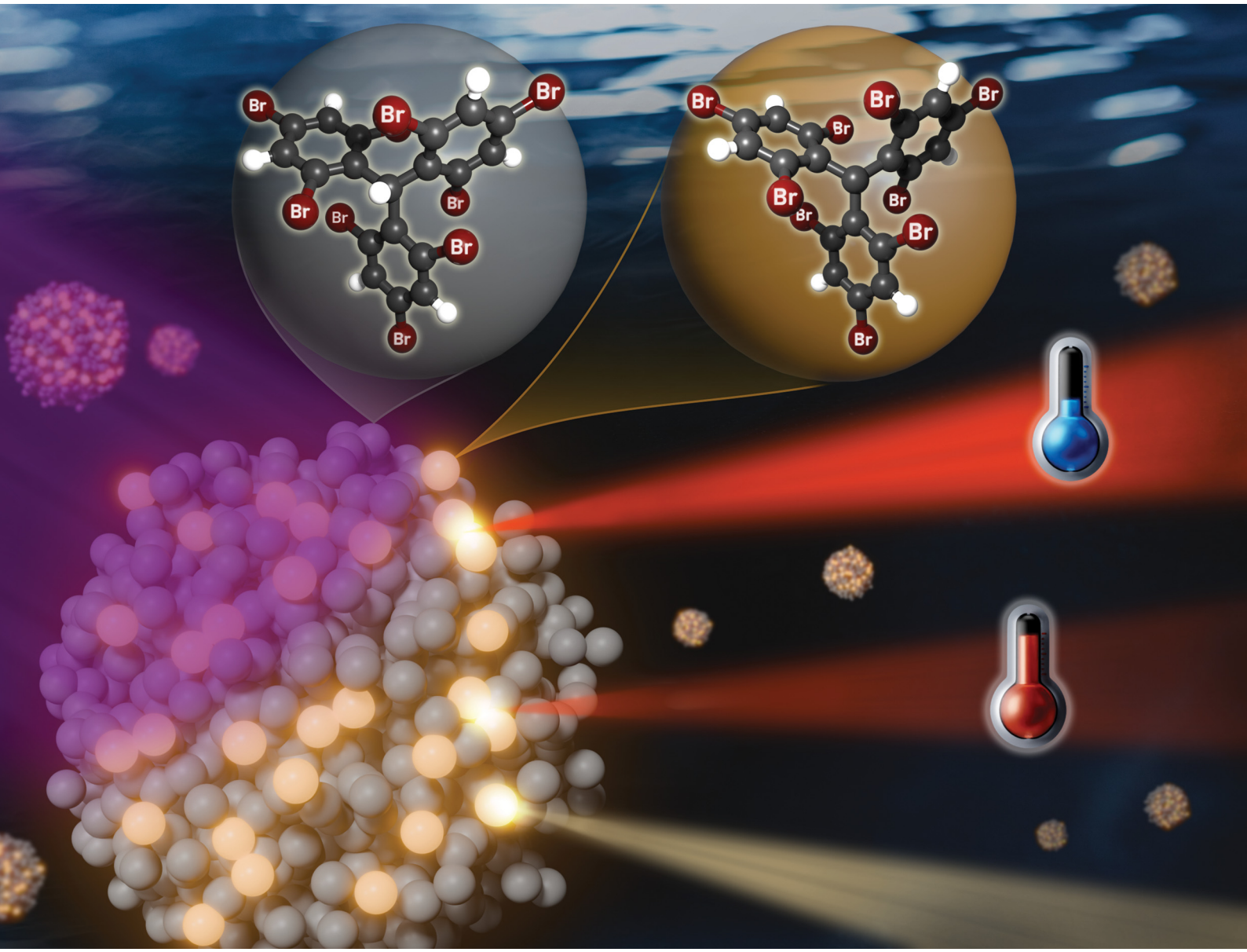

ISSN 2050-7526

ROYAL SOCIETY OF CHEMISTRY

PAPER

Paula Mayorga-Burrezo, Imma Ratera *et al.*
Brominated trityl radical nanoparticles: metal-free ratiometric nanothermometer with near-infrared excimeric emission in water

Journal of Materials Chemistry C

ROYAL SOCIETY OF CHEMISTRY

PAPER

View Article Online
View Journal | View Issue

Cite this: J. Mater. Chem. C, 2025, 13, 23392

Brominated trityl radical nanoparticles: metal-free ratiometric nanothermometer with near-infrared excimeric emission in water

Nerea Gonzalez-Pato, †[ab] Giovanni Schievano, †[a] Pau Armada, [c] Jesús Cerdá, [d] Davide Blasi, ‡[a] Juan Aragó, [c] Jaume Veciana, [ab] Paula Mayorga-Burrezo *[ab] and Imma Ratera *[ab]

Received 22nd July 2025,
Accepted 22nd September 2025

DOI: 10.1039/d5tc02784e

rsc.li/materials-c

The development of efficient, metal-free luminescent nanothermometers operating near the first near-infrared (NIR-I) biological window is crucial for advancing biomedical imaging and temperature sensing at the nanoscale. In this work, we report a new family of brominated organic radical nanoparticles (**Br-ONPs**), prepared by nanoprecipitation of a persistent tris(2,4,6-tribromophenyl)methyl (TTBrM) radical doped into its optically inert precursor matrix (TTBrM-αH). Aqueous dispersions of **Br-ONPs** exhibit high colloidal stability, sizes below 130 nm, and dual emission under a single excitation. Thus, in addition to the emission of isolated monomeric TTBrM radicals inside the matrix, an excimeric band emerges at doping ratios ≥15 wt% due to simultaneous formation of TTBrM dimers with short intermolecular contacts inside the matrix which are similar to those present in crystalline polymorphs. Compared to chlorinated analogues (**Cl-ONPs**), **Br-ONPs** show the desired red-shift in both monomer and excimer emissions, entering into the interesting NIR-I window. Theoretical calculations support the electronic origin of the excimer emission and the role of bromine in modulating the optical properties. Temperature-dependent fluorescence studies confirm the suitability of metal-free **Br-ONPs** as a novel and efficient ratiometric nanothermometer in aqueous environments, with tunable optical output. Altogether, these findings not only establish **Br-ONPs** as promising candidates for future *in vivo* bioimaging applications, but also provide valuable insights into the design principles and key parameters governing the performance of organic nanothermometers.

Introduction

As modern electronics grow increasingly compact and powerful, effective thermal management has become a key concern, with hot spots formation within device architectures jeopardizing their functionality and reducing their operational lifespan. This trend has driven strong interest in the design of efficient nanothermometers capable of sensing temperature variations within the submicrometric region and with optical outputs.[1,2] Nonetheless, not only the field of electronics is fuelling the progress in nanothermometry but also the field of biomedicine. Nanothermometry has also become a major technology for advancing biomedical research given that an accurate cellular temperature information is vital to fully understanding life science processes.[3,4] Promising performances of luminescent thermoresponsive nanoparticles (NPs) with precise temperature spatial and time resolution have been reported,[5] allowing the investigation of metabolic processes[6,7] or monitoring heat-based treatment in cancer therapy.[8] However, several limitations are hindering the broader application of light emission as a thermometric signal.[9]

Ratiometric luminescence systems have nevertheless emerged as reliable candidates for remote thermal mapping at the nanoscale, where conventional thermometers fail. Biological tissues, for instance, are not transparent and often exhibit autofluorescence in the visible range. Moreover, non-temperature related factors, such as the concentration of the dye or the excitation power dependence,[10] can also affect the performance of the emissive NPs. These constraints have

[a] Institute of Material Science of Barcelona (ICMAB-CSIC), Bellaterra, 08193, Spain. E-mail: pmayorga@icmab.es, iratera@icmab.es
[b] Networking Research Center on Bioengineering, Biomaterials and Nanomedicine (CIBER-BBN), Bellaterra, 08193, Spain
[c] Instituto de Ciencia Molecular (ICMol), Universitat de València, Catedrático José Beltrán 2, Paterna 46980, Spain
[d] Laboratory for Chemistry of Novel Materials, Université de Mons, Mons 7000, Belgium
† These authors contributed equally.
‡ Current address: Dipartimento di Chimica, Universitá degli Studi di Bari Aldo Moro, Via Edoardo Orabona 4, Bari 70126, Italy.

underscored the value of ratiometric luminescence systems in overcoming such challenges.[10–13] Many examples of nanothermometers involving core shell metal organic particles with two dyes[14–16] or quantum dots[11,16] have appeared in the recent literature, describing their ability to provide absolute measurements of temperature variations based on the ratio of fluorescence emission at two different wavelengths. Nonetheless, it is worth noting that the rapid evolution of the field has been mainly fuelled by lanthanide-based candidates owing to their ability to operate within the near-infrared NIR-I (700–950 nm) and NIR-II (1000–1700 nm) biological windows,[17–23] where reduced photon scattering and absorption processes enable an enhanced light penetration into biological tissues. Despite their significant impact on nanothermometric imaging technologies, lanthanide derivatives still pose possible concerns, including inconsistent *in vivo* toxicity and unclear long-term safety profiles.[24–26] Alternatively, metal-free organic compounds, with easy tuneable excitation and emission wavelengths, can significantly enhance biocompatibility too. With such compounds, several strategies have been developed to construct organic ratiometric nanothermometers suitable for aqueous environments. For instance, two organic fluorophores of dissimilar thermoresponsiveness can be embedded in polymeric NPs that prevent their leakage.[27,28] Another approach involves the use of temperature-sensitive polymeric matrices undergoing phase transitions to encapsulate stimuli-responsive organic emitters (*e.g.*, to molecular state of aggregation,[29,30] or water presence[31]). Unfortunately, the phase transitions in the polymeric matrices usually occur in a narrow temperature interval which, in turns, produce an abrupt modification of the fluorescent signal instead of progressive variation.

In recent studies within this area, some of us have demonstrated the potential of the stable tris(2,4,6-trichlorophenyl)methyl radical (TTM)—a persistent halogenated triarylmethyls (trityl) radical derivative—for application in ratiometric NIR-nanothermometry. Briefly, the TTM was used as dopant within an optically neutral matrix made of its hydrogenated precursor, tris(2,4,6-trichlorophenyl)methane (TTM-αH), to prepare a water suspension of nanoparticles by the re-precipitation methodology.[32–34] The resulting aqueous dispersion of stable radical-based organic nanoparticles (TTM-ONPs) exhibited an intrinsic dual emission thanks to the generation of an excimeric emissive state in the region close to NIR at 567–665 nm, as a consequence of the proximity of the radical neighbouring molecules within the ONPs.[32] The temperature dependence of the excimeric emission in the TTM-ONPs favoured the development of a reliable, non-cytotoxic, metal-free nanoscale temperature sensor,[32] which has been validated *in vivo*,[33] and under two-photon excitation conditions in biological tissues.[34] Unfortunately, the emissions of TTM-ONPs are still far from the NIR-I biological window thereby limiting some bioapplications. At this point, it is important to stress that the above-mentioned properties are not generalizable to trityl radicals, including many bearing different chlorinated shields. As a matter of example, the formation of excimers was hindered when a fully chlorinated trityl derivatives, namely perchlorotriphenylmethyl radical (PTM) and its non-radical precursor (PTM-αH), were used for the ONPs preparation because its formation is controlled by subtle competing interactions.[32,34]

In this work, the nanostructuration of an alternative brominated trityl radical derivative will be addressed. As depicted in Scheme 1A, the tris(2,4,6-tribromophenyl)methyl radical (TTBrM)[35] will be combined with its optically neutral counterpart (TTBrM-αH) for the preparation of original brominated ONPs (**Br-ONPs**). Despite the molecular functionalization of the *ortho-* and *para-* positions with bulky bromine atoms, the generation of excimers is intended. In addition, the TTBrM dopant concentration in **Br-ONPs** will be systematically optimized to enhance the dual intrinsic emission under a single excitation wavelength (Scheme 1B). When compared with the chlorinated TTM-ONPs, from now on **Cl-ONPs**, a redshift on the

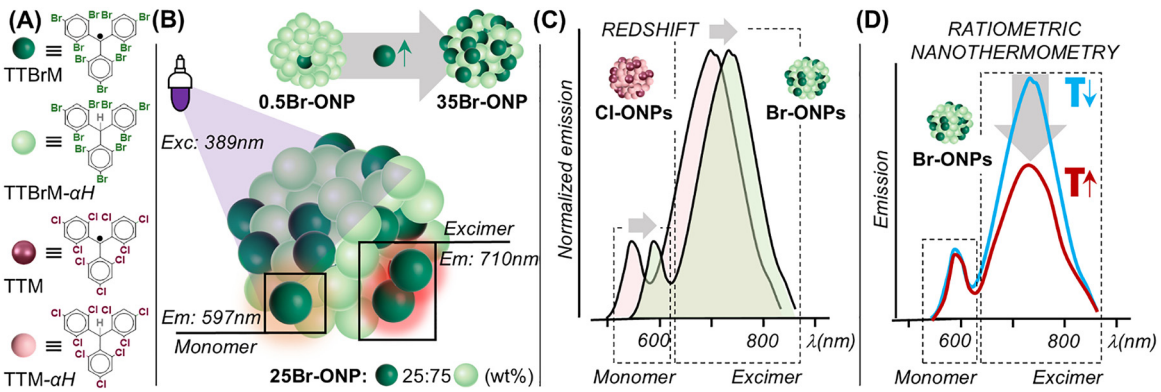

Scheme 1 Ratiometric NIR-nanothermometer based on TTBrM radical. Schematic representation of: (A) the chemical structures of the open-shell TTBrM together with its non-radical precursor (TTBrM-αH) and the chlorinated homologues TTM and TTM-αH, respectively; (B) the brominated trityl radical-based organic nanoparticles (**Br-ONPs**) resulting from the combination of TTBrM and TTBrM-αH. Increasing radical doping ratios, from 3 to 35 wt %, namely **3Br-ONPs** to **35Br-ONPs**, have been explored aiming at the enhancement of the optical properties. The presence of emissive monomer and excimers at higher radical doping ratios (*e.g.*, **25Br-ONPs**) when irradiated with a single excitation wavelength has also been depicted; (C) comparison of the fluorescence spectra of **Br-ONPs** and their homologues **Cl-ONPs**, highlighting the redshift associated with the brominated molecular shields; (D) the temperature dependence of the excimeric fluorescence band in optimized **Br-ONPs** and the derived ratiometric nanothermometric functionality.

emissive properties is expected for the **Br-ONPs** (Scheme 1C), as in the case of the emission spectra of the molecular radicals in solution.[35] Thus, **Br-ONPs** are developed to enhance suitability for biomedical use, better meeting the criteria required for applicability near the biological NIR-I transparency window. Theoretical calculations will also be performed to address the impact of the brominated molecular shields on the formation of excimeric states and the effect over the optical properties. Finally, the performance of optimized **Br-ONPs** as ratiometric NIR-nanothermometers in aqueous media will be tested (Scheme 1D).

Results and discussion

Synthesis, crystal structure and organic nanoparticles (ONPs) preparation

Tris(2,4,6-tribromophenyl)methane (TTBrM-αH) and tris(2,4,6-tribromophenyl)methyl radical (TTBrM) were synthetized in line with previous reported procedures (see SI for further details).[35] The obtained TTBrM was successfully crystallized, and two different polymorphs were identified. One corresponds to a previously reported structure described by some of us, featuring platelet-like crystals with a minimal C_{meta}–C_{meta} intermolecular distance of 4.092 Å between two neighbouring radical molecules.[35] In addition, a new polymorph was discovered in the form of needle-shaped crystals and exhibiting a shorter C_{meta}–C_{meta} distance of 3.802 Å (Fig. S2, S3 and Tables S1, S2). This value is comparable to that observed for TTM crystals (*i.e.*, 3.854 Å)[36] that is known to form excimers when used to generate radical doped organic nanoparticles[33] (Fig. S3). Both polymorphs exhibit intermolecular distances shorter than those observed in the PTM crystals (*i.e.*, 4.237 Å), which do not form excimers when incorporated in their respective organic nanoparticles.[34] This suggests that TTBrM, despite having a larger atomic radius, may also be capable of forming excimers like TTM. Further structural details are provided in the SI.

The preparation of the water suspension of **Br-ONPs** was done following the optimized re-precipitation methodology reported for **Cl-ONPs** (See SI).[32–34] Given that pure emissive trityl radicals exhibit a complete aggregation-caused quenching (ACQ) of fluorescence,[32] a comprehensive library of aqueous suspensions of **Br-ONPs** was generated from the combination of TTBrM and TTBrM-αH to gain further insights into their fluorescence behaviours. As in the case of **Cl-ONPs**, the TTBrM-αH was chosen as a matrix for the ONPs because of: (1) its optically-inactive behaviour in the range of absorption and emission of the TTBrM radical and also (2) the similarities between the radical and non-radical molecular structures, providing good solvation, preventing self-aggregation of the active radical and increasing the concentration quenching of the luminescence. The radical content, or TTBrM doping ratio, was varied as follows: 3 wt% (**3Br-ONPs**), 15 wt% (**15Br-ONPs**), 20 wt% (**20Br-ONPs**), 25 wt% (**25Br-ONPs**), and 35 wt% (**35Br-ONPs**). Spherical-shaped ONPs were observed by transmission electron microscopy (TEM) imaging for the resulting dispersions (Fig. 1A).[32] Dynamic light scattering (DLS) measurements showed sizes between 80 and 130 nm for all the **Br-ONPs** water colloidal dispersions and a polydispersity index (PDI) below 0.2 for all of them, which is indicative of the high homogeneity of the ONP suspensions. A modest decrease in the particle size is observed as the percentage of radical doping inside the ONPs increase (Fig. 1B). Moreover, a slightly average increase of particle size of 7.5% was observed across all dispersions after approximately 6 months (Fig. S4). In any case, all samples displayed negative surface potential values of around −40 mV (Fig. 1C) ensuring very good colloidal stability. Electron paramagnetic resonance (EPR) measurements were also conducted to gain further insight into the fate of the unpaired electrons in the radical molecules. A successful transfer of the magnetic activity from the TTBrM to the water compatible nanoassemblies was confirmed by the EPR signals recorded at room temperature from aqueous **Br-ONPs** suspensions. As exemplified by the **20Br-ONPs** sample (g = 2.0065, Fig. S5), g values close to that of the free electron were observed in all cases. However, the significantly higher value than the one reported for **Cl-ONPs** (g: 2.0030),[33] was attributed to the increased spin–orbit coupling associated with the presence of the bromine atoms. As for the optical properties, a reported mathematical treatment[37] was applied to correct the scattering of the UV-Vis electronic absorption spectra of the **Br-ONP** suspensions in water (see, for instance, **25Br-ONPs** in Fig. 1D). The characteristic C band of

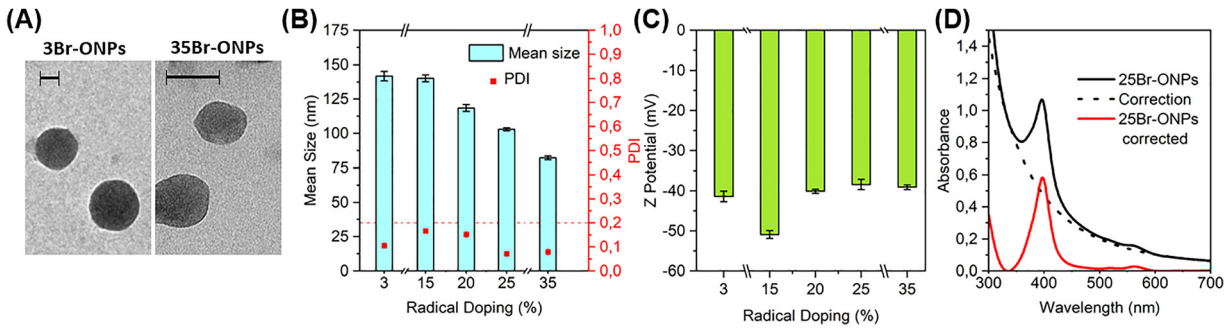

Fig. 1 **Br-ONPs** characterization. (A) Representative TEM image of **3Br-ONPs** (left) and **35Br-ONPs** (right). Scale = 50 nm in both cases; (B) hydrodynamic diameter evolution, polydispersity (PDI) index and (C) Z-Potential distribution with increasing TTBrM doping ratio of the **Br-ONPs**; (D) UV-Vis electronic absorption spectra of **25Br-ONPs** water dispersion before (black) and after (red) the mathematical treatment for scattering correction.

trityl derivatives, attributed to delocalization of the unpaired electron across the aromatic rings, was clearly observed at 389 nm, in line with the reported data for the isolated molecule (Fig. S6B).[35] In contrast, a red shift of 10 nm was detected when comparing **20Br-ONPs** to analogous **20Cl-ONPs** (TTM-based ONPs with a radical content of 20% w/w, Fig. S6A). This experimental fact was attributed to the substitution of chlorine with bromine atoms in the halogenated shields of both the radical and non-radical molecules comprising the ONPs.

Emissive properties of Br-ONPs: excimer formation

With the successful nanostructuration of TTBrM radicals into **Br-ONPs**, their fluorescence behaviours were subsequently examined to complete their characterization. To this end, emission spectra for each aqueous dispersion were recorded under a fixed wavelength excitation (λ_{exc} = 390 nm) at room temperature. As depicted in Fig. 2, the spectra of **Br-ONPs** with low radical doping ratios (*i.e.*, 3%) only showed a main emission band at 597 nm, in line with the fluorescence spectrum of the isolated TTBrM in solution.[35] At such low concentration of TTBrM radical, the molecules inside the **Br-ONPs** should be completely isolated, avoiding the aggregation-caused quenching (ACQ) and also too far apart to electronically interact effectively, preventing the formation of optically active excimers. A significant drop in the emission intensity of the monomer contribution was observed for the ONPs with doping ratios above 15%. With the increase of radical doping, an additional band appear at longer wavelengths (*i.e.*, 710 nm), which is attributed to the presence of excimeric species in line with the fluorescence spectra obtained for **Cl-ONPs** under the same experimental conditions.[33] Thus, it was demonstrated that the bulkiness of the brominated shield in TTBrM did not hinder the generation of excimeric species in **Br-ONPs** but provoked an interesting red-shift in the overall emission spectrum, as noticed when compared with the chlorinated counterpart (**20Cl-ONPs**/**Br-ONPs**: 567/597 nm and 665/710 nm, see Fig. S7).

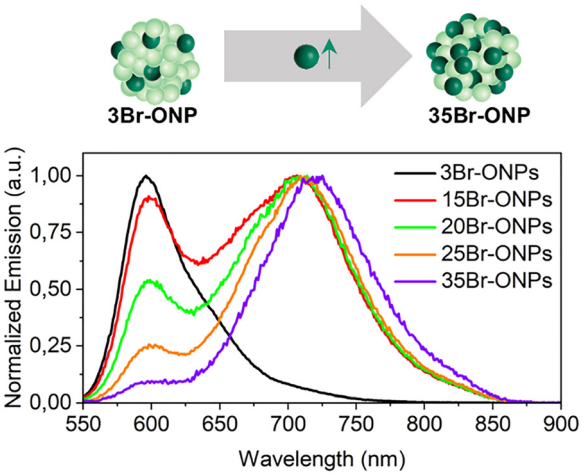

Fig. 2 Fluorescence behaviour of **Br-ONPs**. Normalized emission spectra of **Br-ONPs** suspensions at different % of TTBrM content. Experimental details: all the water suspensions were measured at 20 °C and at a single excitation wavelength (λ_{exc}) at 390 nm.

Both **Cl-ONPs** and **Br-ONPs** therefore reproduce the optical properties of the two molecules in solution.[35] A comparison of the fluorescence quantum yield (FQY) values of the two formulations, the chlorinated and brominated ONPs, was also run, showing a similar trend to the one reported for the isolated radicals in viscous organic solutions (see Table S3).[32,35] The less electron-withdrawing nature of the Br atoms may account for the lower yield compared to TTM. Finally, for high % of radical doping inside the **Br-ONPs** a quenching of fluorescence emission was observed (see Fig. S8). This effect was especially pronounced at doping ratios above 25%, in line with the expected ACQ of fluorescence when the radical molecules are not isolated. Fig. S8A shows the two competitive phenomena controlling the intensity of the fluorescence emission of the **Br-ONPs** water suspension as the radical doping %; on one side, the excimeric emission increases at 710 nm and, on the other side, the ACQ affecting the monomer emission, as well as the excimeric emission in the case of radical dopings higher than 25%.

To further understand the difference between the optical properties of both **Cl-** and **Br-ONPs**, a combined theoretical approach was employed, using electronic structure calculations, a powerful multistate diabatization scheme[38] and a model Hamiltonian to simulate the emission spectra of the monomer and dimer species of TTM and TTBrM (see SI for a detailed explanation). Briefly, the approach started with excited states calculations at the time-dependent density functional theory based on the crystal structures of the monomeric and dimer species of TTM and TTBrM (Fig. S13 and Tables S7, S8) to estimate the energy position of the relevant low-lying Frenkel (FE) and charge-transfer (CT) excited states. An optimally-tuned LC-ωhPBE functional (ω = 0.11 Bohr^{-1})[39–41] in combination with the 6-31G** basis set was employed for the excited state calculations,[42] performed with the Gaussian 16 A.03 software package[43] (see SI for additional details). Further geometry optimizations of the FE- and CT-type excited states in monomer and/or dimer species of TTM and TTBrM were also performed to estimate the adiabatic energies that are included in the model Hamiltonian. This theoretical characterization is essential since the excimer formation in molecular dimers requires a substantial mixing between FE and CT states along with a significant structural relaxation (mostly due to intermolecular motions).[44–46] A brief analysis of the structural changes for the optimized FE and CT states is given in SI (Table S4 and Fig. S10). The electronic structure calculations were finally employed to parameterize the model Hamiltonian, which is based on a Holstein–Peierls Hamiltonian that includes local and no local exciton-vibrational couplings and electronic excitations of FE- and CT-type character. Note that this vibronic Hamiltonian has been recently proposed by Spano and co-workers to successfully describe the emission spectra in molecular excimers.[46,47]

Fig. 3A shows a scheme of the important FE and CT excited (diabatic) states along with the vibrational levels (close in energy) incorporated in the model Hamiltonian for the excimer formation. Fig. 3B compares the simulated emission spectra for the different species (monomer or/and dimer) of TTM and

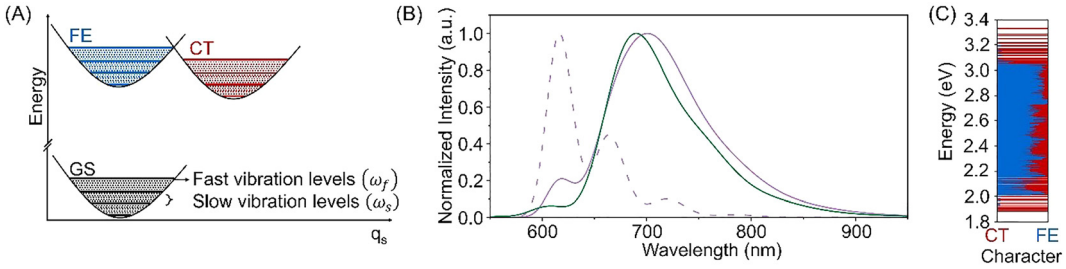

Fig. 3 (A) Scheme of the relevant pure Frenkel (FE) and charge-transfer (CT) excited states together with the vibrational levels involved for the excimer formation. (B) Comparison of the simulated emission spectra for the TTBrM monomer (dotted purple), TTBrM dimer (purple) and TTM dimer (green) at room temperature (20 °C). (C) Nature of the vibronic emitting eigenstates (FE and CT character) for the TTBrM dimer.

TTBrM whereas Fig. 3C displays the nature of the emissive vibronic eigenstates. For TTBrM (Fig. 3B), the simulated fluorescence spectrum for the monomer exhibits an emission band with a distinguishable vibrational structure (peaked at 617, 664 and 720 nm) whereas the fluorescence spectrum for the dimer is significantly different with two well-separated emission bands, a weak band predicted in the region of the monomeric radical (619 nm) and a dominant broad and red-shifted emission band (701 nm) characteristic of the excimer formation. The shape of the fluorescence spectra calculated for both the monomeric and dimer species are in good agreement with those experimentally reported in Fig. 2 at the lowest and highest radical doping ratio. Note that, at lowest radical doping ration, all the spectral signal come from the radical monomer whereas, at the highest radical doping ration, the spectral signatures would mainly arise from excimeric species (dimers). The theoretical findings therefore underpin that, despite the bulkier size of bromine compared to chlorine, TTBrM can give rise to excimers within the **Br-ONPs.** Likewise, the comparison of the simulated emission spectra for TTM and TTBrM dimers clearly highlights that the excimeric emission for TTBrM is red-shifted compared to TTM in line with the experimental evidences (Fig. S7). This arises because the relevant FE and CT excited states for TTBrM dimer are predicted at slightly lower energies than those found for TTM (Table S4).

Thermometric performance of Br-ONPs

The thermometric performance of **Br-ONPs** with different TTBrM radical doping % (**15Br-ONPs**, **20Br-ONPs**, **25Br-ONPs** and **35Br-ONPs**) was investigated through temperature-dependent emission measurements under 390 nm excitation (Fig. 4A and Fig. S9A–D). All samples display dual emission bands corresponding to the monomer (597 nm) and excimer (710 nm) transitions. As the temperature increases from 5 °C to 55 °C, a gradual decrease in excimer emission is observed across all samples, accompanied by a relatively stable or slightly increasing monomer signal (Fig. S9E–H), confirming a ratiometric thermometric response.

This behaviour correlated well with the simulated emission spectra of TTBrM dimers at different temperatures (Fig. 4B). As temperature increases, a decrease in the broad excimer band and a slight increase in the monomer-like emission band were predicted, consistent with the thermal population of the

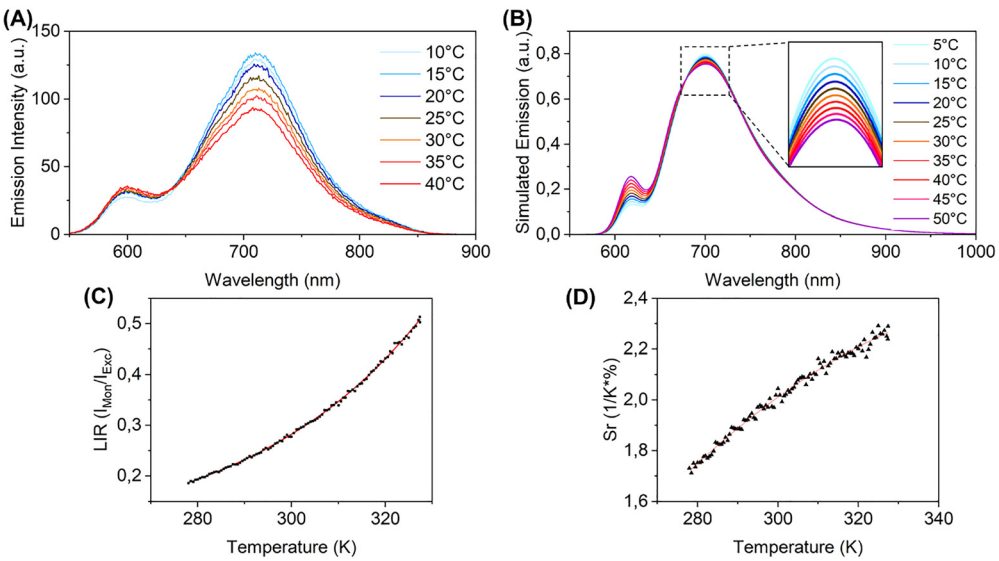

Fig. 4 **Br-ONPs** as ratiometric nanothermometers. (A) Representative emission spectra of **25Br-ONPs** at different temperatures, (B) simulated emission spectra of TTBrM dimer as a function of temperature, (C) LIR calculated (dots) and plotted (red line) between 5 and 55 °C and (D) relative sensitivity calculated from individual points (dots) and from eqn (1) (red line).

Table 1 Comparison of thermometric properties between **25Br-ONPs** and **20Cl-ONPs**

Parameter	**25Br-ONPs**		**20Cl-ONPs**[33]	
Temperature	25 °C	37 °C	25 °C	37 °C
Monomer emission	597 nm	597 nm	567 nm	567 nm
Excimer emission	710 nm	710 nm	665 nm	665 nm
S_r (%K^{-1})	1.98	2.12	1.89	2.13
ΔT_{min} (K)	0.18	0.13	0.18	0.13

S_r: relative sensitivity; ΔT_{min}: minimum temperature interval detectable $\Delta T_{min} = \frac{\sigma(LIR)}{S_a}$[K].

emissive vibronic states (Fig. S11). At low temperatures, the dominant emissive states exhibit a charge-transfer (CT) character with a slight FE-type contribution as illustrated in Fig. 3C. Although minor, this FE contribution is crucial as it endows these states with optical activity (pure CT states typically lack significant oscillator strength and pure diabatic FE vibronic states are the only ones that carry non-negligible oscillator strengths). At higher temperatures, there is a tiny population transfer to vibronic states with a more FE-type nature (monomer-like) and, consequently, the emission band intensities at the radical and excimer species increase and decrease, respectively (Fig. 3, 4B and Fig. S11), as observed experimentally.

To quantitatively describe this thermal behaviour, the luminescence intensity ratio (LIR) was also calculated as LIR = I_{Mon}/I_{Exc} across the entire temperature range, and fitted using the empirical relation LIR = $a + b \times e^{cT}$,[33,34,48] where I_{Mon} and I_{Exc} correspond to the emission intensities of the monomer and the excimer, respectively (Fig. 4C and Figure S9I). All systems follow a sigmoidal trend, successfully fitted using eqn (1). In addition, the relative sensitivity was calculated over the full temperature interval, using eqn (1) (Fig. 4D and Fig. S9K).

The absolute sensitivity (S_a) (Fig. S9J) reaches its maximum for **20Br-ONPs** but the relative sensitivity (S_r), shown in Fig. S9K, peaks for **25Br-ONPs** particularly considering their lower signal variability, reinforcing their potential for biological applications. In terms of thermal resolution, **25Br-ONPs** also display the lower temperature uncertainty (ΔT_{min}) among the series (Fig. S9L).

$$S_r = \frac{d(LIR)}{dT}\frac{1}{LIR} \times 100\%\left[\% \times K^{-1}\right] \quad (1)$$

Altogether, these results highlight the strong influence of TTBrM content on thermometric performance, with **25Br-ONPs** emerging as the optimal formulation based on multiple criteria: higher luminescence intensity (before significant quenching), enhanced monomer-to-excimer emission ration, high sensitivity, and excellent temperature resolution within the physiological range (Fig. 4A). It is worth noting that the sensitivity of **25Br-ONPs** remains consistently between 1.8 and 2.3% K^{-1} within the physiologic temperature range values well above the commonly accepted threshold of 0.5%K^{-1} for efficient nanothermometers.

Same methodology was followed to test the thermometric properties of **20Cl-ONPs**, composed of TTM radical, in previous works.[33,34] Table 1 shows the differences in thermometric and optical performances of the two metal-free radical-based nanoparticles. Compared with **20Cl-ONPs**, **25Br-ONPs** are slightly less emissive without affecting significantly their optical-based thermometric properties. The lost in emissive capacity can have its origin already at molecular level since the oscillator strengths predicted for the first two excitations of the TTBrM radical are slightly smaller than those obtained for the TTM radical (Table S5). Importantly, new **25Br-ONPs** exhibit a red-shifted spectral profile, further extending their emission and entering into the first biological transparency window, *i.e.* NIR-I region, which makes them particularly attractive for *in vivo* applications.

Conclusions

In this work, we report the successful development of brominated trityl radical-based organic nanoparticles (**Br-ONPs**) as fully organic, ratiometric nanothermometers operating in the near-infrared region. By nanostructuring the TTBrM radical with its optically neutral and non-radical precursor, TTBrM-αH, we achieved water-dispersed ONPs exhibiting dual emission from monomeric and excimeric states under a single excitation wavelength. A systematic variation of the radical content enabled the tuning of the emission properties, with excimer formation emerging above 15 wt% doping. Compared to their chlorinated analogues (**Cl-ONPs**), **Br-ONPs** show red-shifted emission, entering the NIR-I biological window, while retaining colloidal and photophysical stability. Structural analyses revealed that, despite the increased bulkiness of bromine atoms, intermolecular distances remained favourable for excimer formation, as supported by crystallographic and spectroscopic data. Importantly, the excimer band in **Br-ONPs** exhibited a temperature-dependent intensity, validating their applicability as ratiometric luminescent nanothermometers in aqueous mediawith a nanothermometric sensitivity (S_r) of 1.8–2.3% K^{-1}. Therefore, these findings prove that **Br-ONPs** preserve the key advantages of trityl-based nanothermometry, such as high photostability, ratiometric response, and water dispersibility, while providing improved emission characteristics for biological imaging. Their fully organic composition and red-shifted emission open new opportunities for the generation of robust, biocompatible, and efficient temperature-sensing platforms for advanced biomaging and thermal sensing applications in complex environments. Moreover, the rationalization based on the theoretical calculations implemented in this work will serve as a valuable tool for the future design of optimized thermometric nanoparticles for biological applications.

Author contributions

N.G.-P. and G.S carried out all the activities related to the synthesis and characterization of the ONPs. P. A., J. C. and J. A. where in charge of the theoretical calculations. D. B. carried out preliminary preparation of ONPs and evaluation of optical properties. J.V and I.R originated the idea and P.M.-B. and I.R. supervised the project. P.M.-B. and I.R wrote the

manuscript with inputs from the rest of the authors. All authors have given approval to the final version of the manuscript.

Conflicts of interest

There are no conflicts to declare.

Data availability

All relevant data, including physicochemical characterization, TEM images, DLS measurements, luminescence spectra, EPR, crystal structures, stability studies and theoretical details, are provided in the article and its supplementary information (SI) files. Supplementary information is available. See DOI: **https://doi.org/10.1039/d5tc02784e**.

Additional specific data supporting the findings of this study and data from previously published articles, are available from the corresponding author upon reasonable request. Additional experimental data are available free of charge in a PDF file.

CCDC 2473686 contains the supplementary crystallographic data for this paper.[49]

Acknowledgements

Financial support by European Union (COST Action CA22131 – LUCES and the H2020-MSCA-RISE-2020 project Micro4Nano with Grant Agreement No. 101007804), MICIU/AEI of Spain (PID2022-137332OB-I00, PID2021-128569NB-I00, CNS2022-135187, CEX2024-001467-M and CEX2023001263-S, funded by MICIU/AEI/10.13039/501100011033, ''ERDF A way of making Europe'', and by the ''European Union NextGeneration EU/PRTR''), the Generalitat Valenciana (grant no. MFA/2022/017), and the Generalitat de Catalunya (2021 SGR 438) is acknowledged. This study has been also supported by the Networking Research Center on Bioengineering, Biomaterials and Nanomedicine (CIBER-BBN), an initiative funded by the VI National R&D&I Plan 2008–2011, Iniciativa Ingenio 2010, Consolider Program, CIBER Actions and financed by the Instituto de Salud Carlos III with assistance from the European Regional Development Fund. Project MFA/2022/017 forms part of the Advanced Materials program supported by MICIU with funding from European Union NextGenerationEU (PRTR-C17.I1) and by Generalitat Valenciana. Nerea Gonzalez-Pato acknowledges the financial support from the FPU fellowship (FPU17/02551) from the Spanish Ministry and G.S. acknowledges the financial support from the AEI, PID2022 fellowship (Grant N. PRE2022-000386). P.M.-B. acknowledges financial support from ''la Caixa'' Foundation (ID 100010434), under the agreement ''LCF/BQ/PI23/11970030''. P.A. acknowledges the funding by MICIU/AEI/10.13039/501100011033 and ''FSE +'' (Grant No. PRE2022-101827). J.C. acknowledges to European Union for his Marie Curie Individual fellowship (HORIZON-MSCA-2022-PF-01-01, project no 101106941). This work has been developed within the Materials Science PhD program of the Universitat Autònoma de Barcelona.

We gratefully acknowledge Dr Xavier Fontrodona from the Servei de Cristal·lografia, Universitat de Girona for carrying out the X-ray crystallographic studies reported in this work. It is also acknowledge the assistance of the ICMAB-CSIC Scientific & Technical Services: SOFT, Electron Microscopy (Dr Judith Oró), and Spectroscopy (Victor Vallejo and Dr Vega Lloveras).

References

1 M. A. Kurochkin, D. V. Mamonova, V. A. Medvedev, E. Y. Kolesnikov and I. E. Kolesnikov, *Nanotechnology*, 2024, **35**, 295501.
2 R. Qian, X. Gong, H. Xue, W. Lu, L. Zhu and Z. An, *ES Energy Environ.*, 2019, **6**, 4–17.
3 C. W. Chung and G. S. Kaminski Schierle, *ChemBioChem*, 2021, **22**, 1546–1558.
4 N. Yin, Y. Yu, X. Wang, Y. Shu and J. Wang, *Chem. Eng. J.*, 2024, **490**, 151645.
5 B. del Rosal, E. Ximendes, U. Rocha and D. Jaque, *Adv. Opt. Mater.*, 2017, **5**, 1600508.
6 N. Yin, B. Lin, F. Huo, Y. Shu and J. Wang, *Anal. Chem.*, 2022, **94**, 12111–12119.
7 Y. Takei, S. Arai, A. Murata, M. Takabayashi, K. Oyama, S. Ishiwata, S. Takeoka and M. Suzuki, *ACS Nano*, 2014, **8**, 198–206.
8 R. Piñol, A. Millán, C. D. S. Brites, N. J. Silva and L. D. Carlos, *Nanomaterials for Magnetic and Optical Hyperthermia Applications*, Elsevier, 2019, pp. 139–172.
9 M. Quintanilla, M. Henriksen-Lacey, C. Renero-Lecuna and L. M. Liz-Marzán, *Chem. Soc. Rev.*, 2022, **51**, 4223–4242.
10 J. Zhou, B. del Rosal, D. Jaque, S. Uchiyama and D. Jin, *Nat. Res.*, 2020, **17**, 967–980.
11 Y. Han, Y. Liu, H. Zhao, A. Vomiero and R. Li, *J. Mater. Chem. B*, 2021, **9**, 4111–4119.
12 Y. Wang, Q. Zhang, C. Yang and Z. Xia, *Adv. Mater.*, 2024, **36**, 2401057.
13 M. Liu, J. Liang and F. Vetrone, *Acc. Chem. Res.*, 2024, **57**, 2653–2664.
14 M. Peng, A. M. Kaczmarek and K. Van Hecke, *ACS Appl. Mater. Interfaces*, 2022, **14**, 14367–14379.
15 W. Cao, Y. Cui, Y. Yang and G. Qian, *ACS Mater. Lett.*, 2021, **3**, 1426–1432.
16 Y. Chen, C. Li, T. Yang, E. A. Ekimov, C. Bradac, S. T. Ha, M. Toth, I. Aharonovich and T. T. Tran, *ACS Nano*, 2023, **17**, 2725–2736.
17 N. Jurga, M. Runowski and T. Grzyb, *J. Mater. Chem. C*, 2024, **12**, 12218–12248.
18 Y. Wu, F. Li, Y. Wu, H. Wang, L. Gu, J. Zhang, Y. Qi, L. Meng, N. Kong, Y. Chai, Q. Hu, Z. Xing, W. Ren, F. Li and X. Zhu, *Nat. Commun.*, 2024, **15**, 2341.
19 M. Jia, X. Chen, R. Sun, D. Wu, X. Li, Z. Shi, G. Chen and C. Shan, *Nano Res.*, 2023, **16**, 2949–2967.
20 A. Puccini, N. Liu and E. Hemmer, *Nanoscale*, 2024, **16**, 10975–10993.

21 D. Ananias, F. A. Almeida Paz, L. D. Carlos and J. Rocha, *Chem. – Eur. J.*, 2018, **24**, 11926–11935.
22 M. Tan, F. Li, N. Cao, H. Li, X. Wang, C. Zhang, D. Jaque and G. Chen, *Small*, 2020, **16**, 2004118.
23 M. Zhao, A. Sik, H. Zhang and F. Zhang, *Adv. Opt. Mater.*, 2023, **11**, 2202039.
24 Y.-T. Lin, R.-X. Liu, G. Audira, M. E. Suryanto, M. J. M. Roldan, J.-S. Lee, T.-R. Ger and C.-D. Hsiao, *Toxics*, 2022, **10**, 336.
25 S. Premcheska, A. G. Skirtach and A. M. Kaczmarek, *Adv. Nanobiomed. Res.*, 2025, **5**, 2500003.
26 V. Gonzalez, D. A. L. Vignati, C. Leyval and L. Giamberini, Elsevier Ltd, 2014, preprint, DOI: 10.1016/j.envint.2014.06.019.
27 V. Kalaparthi, B. Peng, S. A. M. A. Peerzade, S. Palantavida, B. Maloy, M. E. Dokukin and I. Sokolov, *Nanoscale Adv.*, 2021, **3**, 5090–5101.
28 Y. Wu, J. Liu, J. Ma, Y. Liu, Y. Wang and D. Wu, *ACS Appl. Mater. Interfaces*, 2016, **8**, 14396–14405.
29 L. Li, C. Zhang, L. Xu, C. Ye, S. Chen, X. Wang and Y. Song, *Angew. Chem., Int. Ed.*, 2021, **60**, 26725–26733.
30 K. Xue, S. Huang, K. Wu, Z. Sun, H. Fu, C. Wang, C. Wang and C. Zhu, *Anal. Chem.*, 2024, **96**, 11026–11035.
31 C. Wang, X. Zhao, K. Wu, S. Lv and C. Zhu, *Biosensors*, 2022, **12**, 702.
32 D. Blasi, D. M. Nikolaidou, F. Terenziani, I. Ratera and J. Veciana, *Phys. Chem. Chem. Phys.*, 2017, **19**, 9313–9319.
33 N. Gonzalez-Pato, D. Blasi, D. M. Nikolaidou, F. Bertocchi, J. Cerdá, F. Terenziani, N. Ventosa, J. Aragó, A. Lapini, J. Veciana and I. Ratera, *Small Methods*, 2024, **8**, 2301060.
34 D. Blasi, N. Gonzalez-Pato, X. Rodriguez Rodriguez, I. Diez-Zabala, S. Y. Srinivasan, N. Camarero, O. Esquivias, M. Roldán, J. Guasch, A. Laromaine, P. Gorostiza, J. Veciana and I. Ratera, *Small*, 2023, **19**, 2207806.
35 P. Mayorga-Burrezo, V. G. Jiménez, D. Blasi, T. Parella, I. Ratera, A. G. Campaña and J. Veciana, *Chem. – Eur. J.*, 2020, **26**, 3776–3781.
36 O. Armet, J. Veciana, C. Rovira, J. Riera, J. Castaner, E. Molins, J. Rius, C. Miravitlles, S. Olivella and J. Brichfeus, *J. Phys. Chem.*, 1987, **91**, 5608–5616.
37 J. Z. Porterfield and A. Zlotnick, *Virology*, 2010, **407**, 281–288.
38 Y.-C. Wang, S. Feng, W. Liang and Y. Zhao, *J. Phys. Chem. Lett.*, 2021, **12**, 1032–1039.
39 T. Körzdörfer and J.-L. Brédas, *Acc. Chem. Res.*, 2014, **47**, 3284–3291.
40 T. Stein, L. Kronik and R. Baer, *J. Am. Chem. Soc.*, 2009, **131**, 2818–2820.
41 T. M. Henderson, A. F. Izmaylov, G. Scalmani and G. E. Scuseria, *J. Chem. Phys.*, 2009, **131**, 044108.
42 M. M. Francl, W. J. Pietro, W. J. Hehre, J. S. Binkley, M. S. Gordon, D. J. DeFrees and J. A. Pople, *J. Chem. Phys.*, 1982, **77**, 3654–3665.
43 M. J. Frisch, G. W. Trucks, H. B. Schlegel, G. E. Scuseria, M. A. Robb, J. R. Cheeseman *et al.*, *Gaussian 16, Revision B.01*, Gaussian, Inc., 2016.
44 Y. J. Bae, D. Shimizu, J. D. Schultz, G. Kang, J. Zhou, G. C. Schatz, A. Osuka and M. R. Wasielewski, *J. Phys. Chem. A*, 2020, **124**, 8478–8487.
45 D. Casanova, *Int. J. Quantum Chem.*, 2015, **115**, 442–452.
46 A. L. Bialas and F. C. Spano, *J. Phys. Chem. C*, 2022, **126**, 4067–4081.
47 H. Haghshenas, A. Bialas and F. C. Spano, *J. Phys. Chem. C*, 2025, **129**, 6397–6413.
48 M. Jia, Z. Sun, M. Zhang, H. Xu and Z. Fu, *Nanoscale*, 2020, **12**, 20776–20785.
49 CCDC 2473686: Experimental Crystal Structure Determination, 2025, DOI: 10.5517/ccdc.csd.cc2p12b5.